Electronic Supplementary Information (ESI)

In situ Formed Graphene Oxide-Polyacrylic Acid Composite Cage on Silicon Microparticles for Lithium Ion Batteries via Esterification Reaction

Chul-Ho Jung, Kyeong-Ho Kim, and Seong-Hyeon Hong*

Department of Materials Science and Engineering and Research Institute of Advanced Materials, Seoul National University, Seoul 151-744, Republic of Korea

* Corresponding author

Prof. Seong-Hyeon Hong (S.-H. Hong)

E-mail: shhong@snu.ac.k

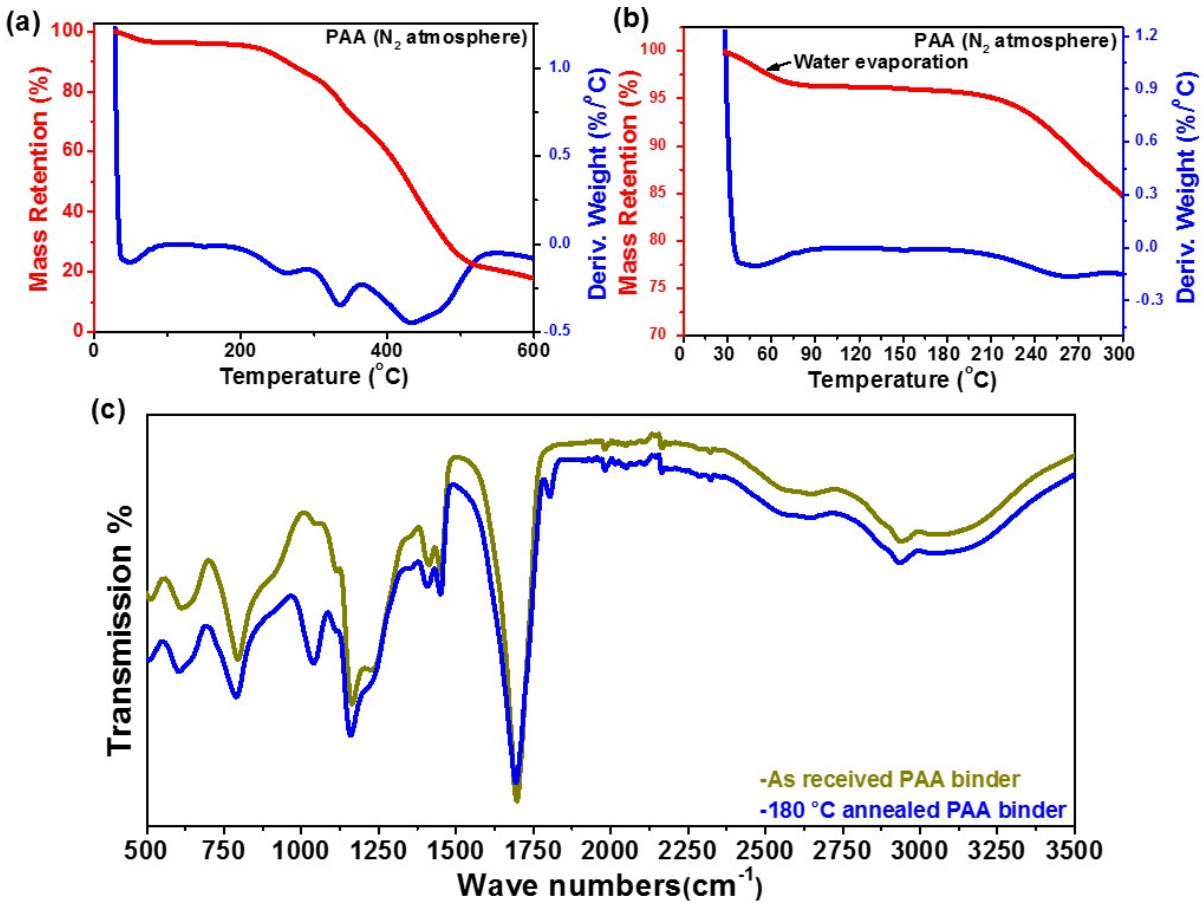

Fig. S1 (a) TGA curve of PAA binder and (b) its magnified image. TGA analysis was conducted under N_2 atmosphere with a heat ramping rate of 10 ^oC min^{-1}. PAA decomposes above 210 ^oC. (c) FTIR comparison between as-received and 180 ^oC annealed PAA binders, in which IR peaks are almost same.

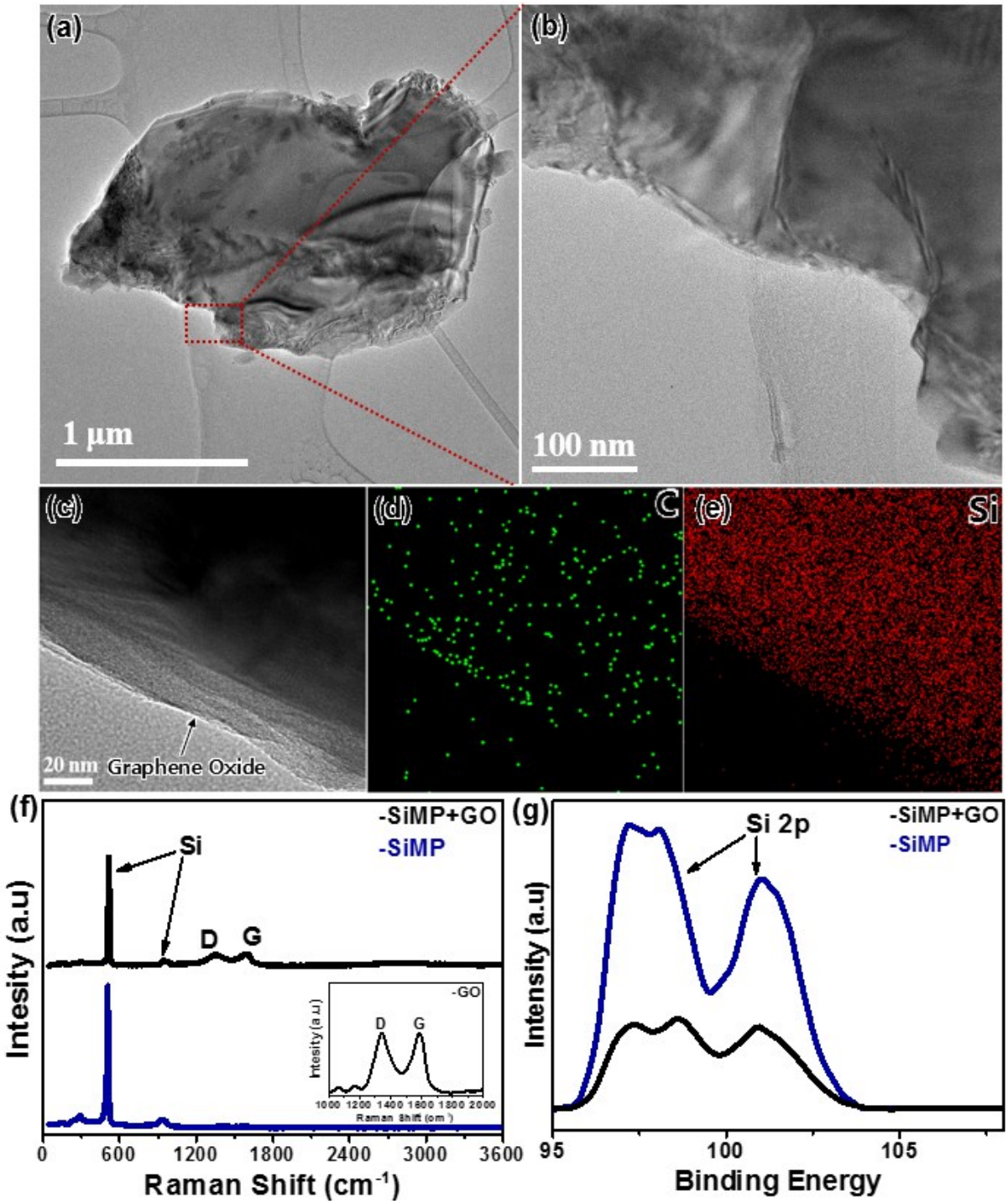

Fig. S2 (a), (b) TEM images of bare SiMPs, (c), (d), (e) TEM and EDS mapping images of [SiMP+GO] composite, and (f) Raman spectra and (g) XPS spectra of bare SiMPs and [SiMP+GO] composite.

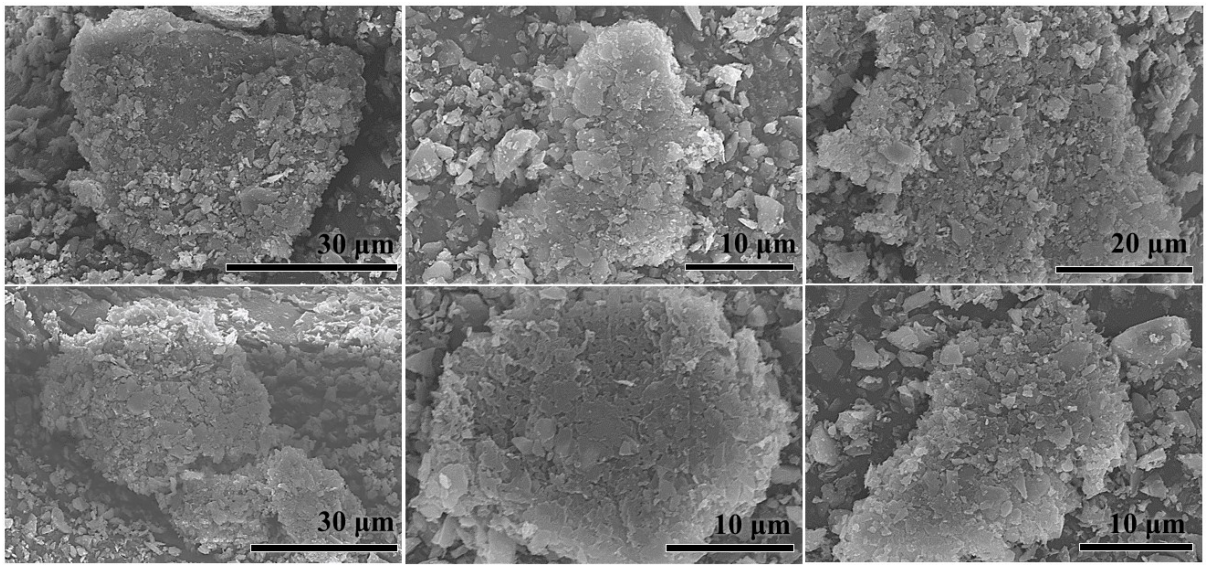

Fig. S3 SEM images of [as-received SiMP+GO] composite where SiMPs were not treated with piranha solution. Due to the difference in surface characteristics of SiMPs (hydrophobic) and GO (hydrophilic), SiMPs and GO are aggregated into 20~30 μm size.

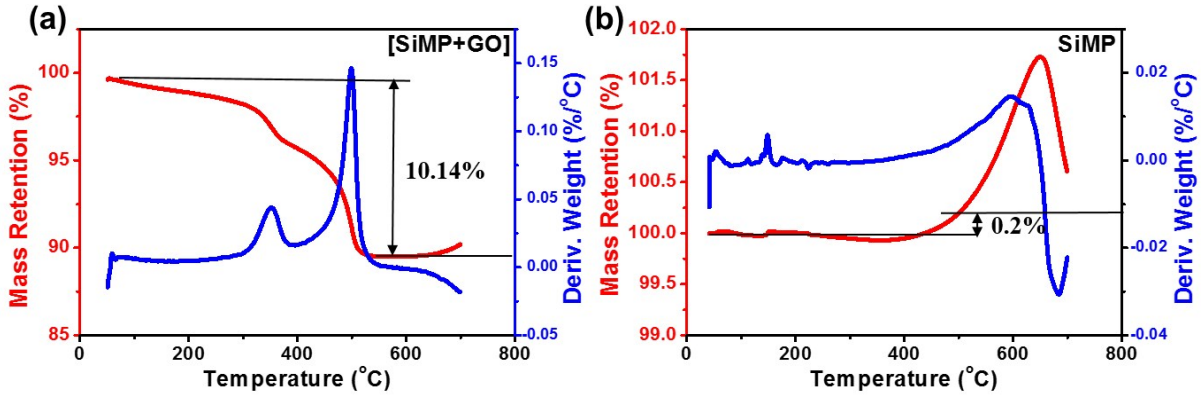

Fig. S4 TGA curves of (a) [SiMP+GO] composite and (b) SiMP conducted in air at a heating rate of 10 °C/min. The weight change of SiMP was 0.2% up to 500 °C and thus, the mass change of [SiMP+GO] composite was mostly derived from the decomposition of GO. The content of GO in [SiMP+GO] composite was ~10%.

Element	Nitrogen	Carbon	Hydrogen	Oxygen
wt %	0.1666	63.064	1.0392	22.0841
at %	0.155	68.4	13.5	17.9

Fig. S5 Carbon/oxygen atomic ratio of GO after annealing at 180 °C determined by elemental analyzer.

Si-based composite	Si content (%)	Charge specific capacity (mAh g^{-1})	Current density (mA g^{-1})	Reference
Micro Si+Graphene	91	3300	210	[1]
Nano Si+Mxene	72.8	1674	840	[2]
Nano Si+TiO_2	89	3061	140	[3]
Nano Si+SnO_2	32.4	1218	100	[4]
Nano Si+CNT	72.5	1500	50	[5]
Nano Si+GaInSn	50	2250	500	[6]
Nano Si+V_2O_5	39	1150	500	[7]
Nano Si+Cupper	X	3305	1000	[8]
Nano Si+Graphite+ Amorphous carbon	12.5	620	60	[9]
Micro Si+GO	89.8	3313	200	This work

Fig. S6 Comparison of lithium storage performance of EB electrode with the previously reported Si-based composites.

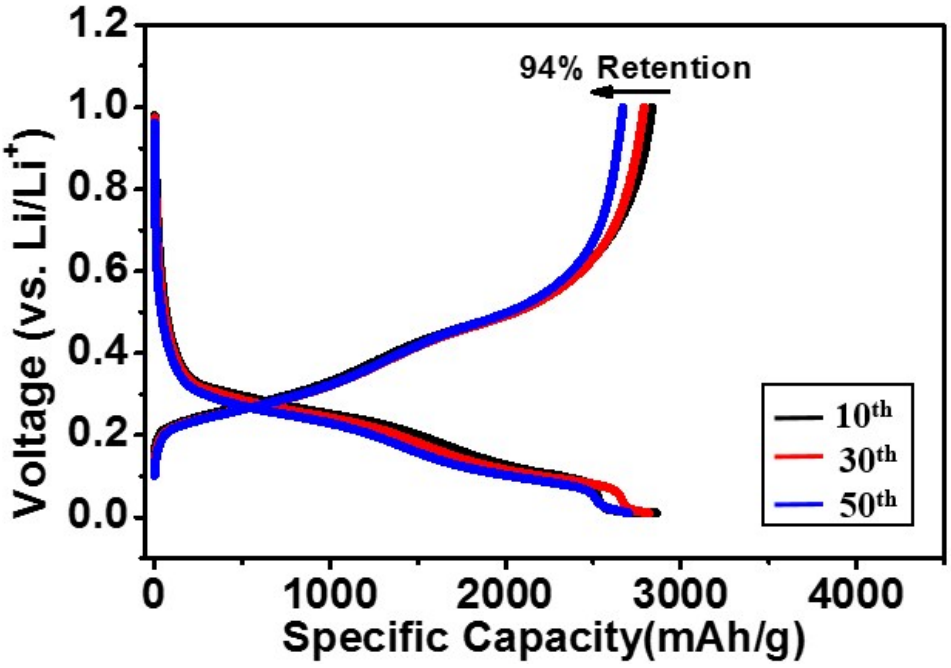

Fig. S7 Galvanostatic graph of EB electrode on Fig. 3c from 10th to 50th cycle.

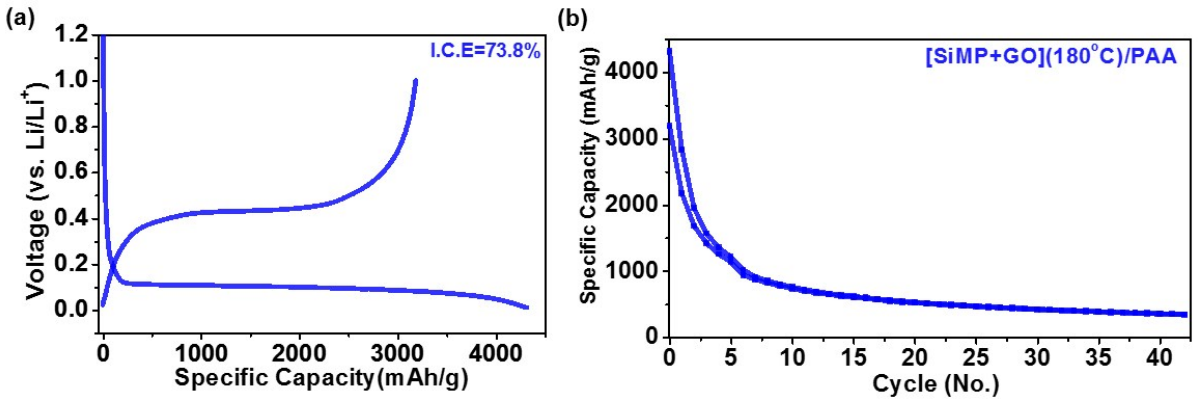

Fig. S8 (a) First charge-discharge voltage profile (b) cycle performance of [SiMP+GO](180°C)/PAA electrode at current density of 1000 mA g^{-1} (one cycle at 200 and 5 cycles at 500 mA g^{-1} for activation process).

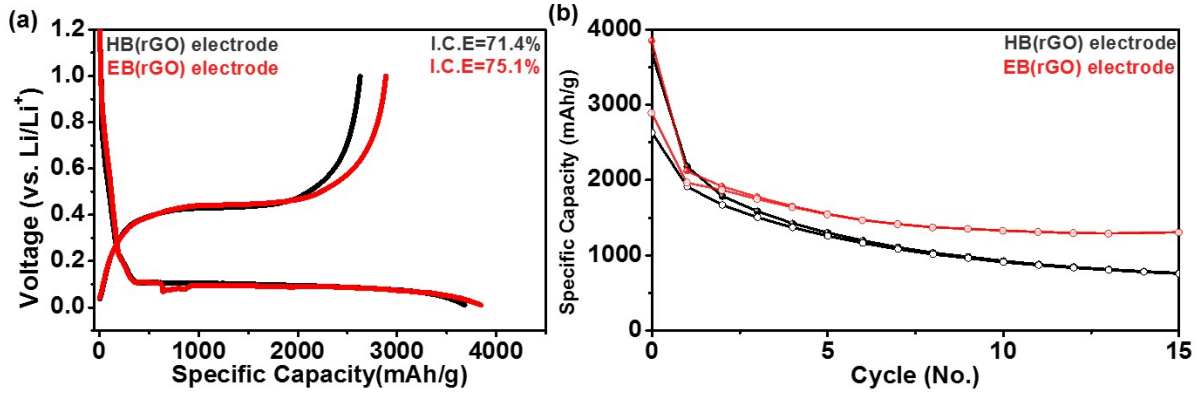

Fig. S9 (a) First charge-discharge voltage profile and (b) cycle performance of HB(rGO) and EB(rGO) electrodes at current density of 1000 mA g^{-1} (one cycle at 200 mA g^{-1} for activation process).

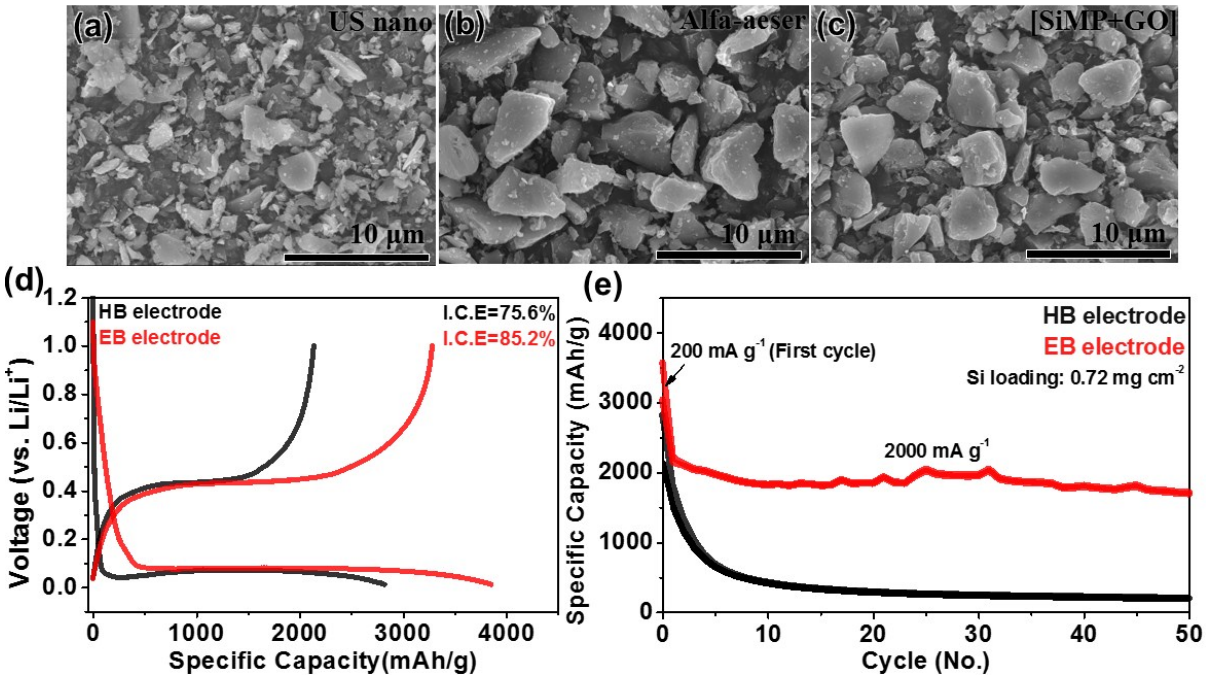

Fig. S10 SEM images of (a) SiMP (US Nano), (b) SiMP (Alfa Aeser), and (c) [SiMP (Alfa Aeser]+GO]. HB and EB electrodes have been fabricated by using [SiMP (Alfa Aeser)+GO] composite. (d) initial charge-discharge voltage profiles for HB and EB electrodes at current density of 200 mA g^{-1}, and (e) cycle performance of HB and EB electrodes at the current density of 200 mA g^{-1} (1 cycle)-2000 mA g^{-1} (subsequent cycles).

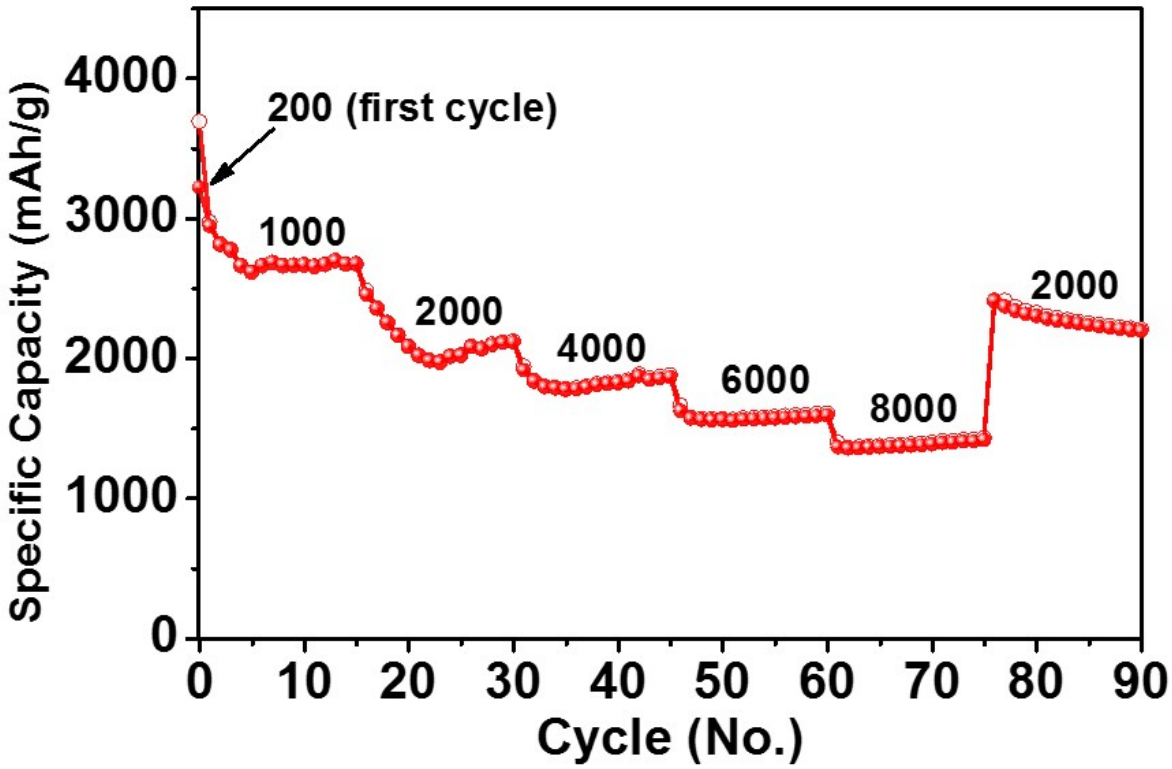

Fig. S11 Rate capability test of EB electrode by increasing the current density from 1000 to 8000 mA g^{-1}. The initially unstable cycling performance upon the change of current density is due to the stabilizing process.[10,11]

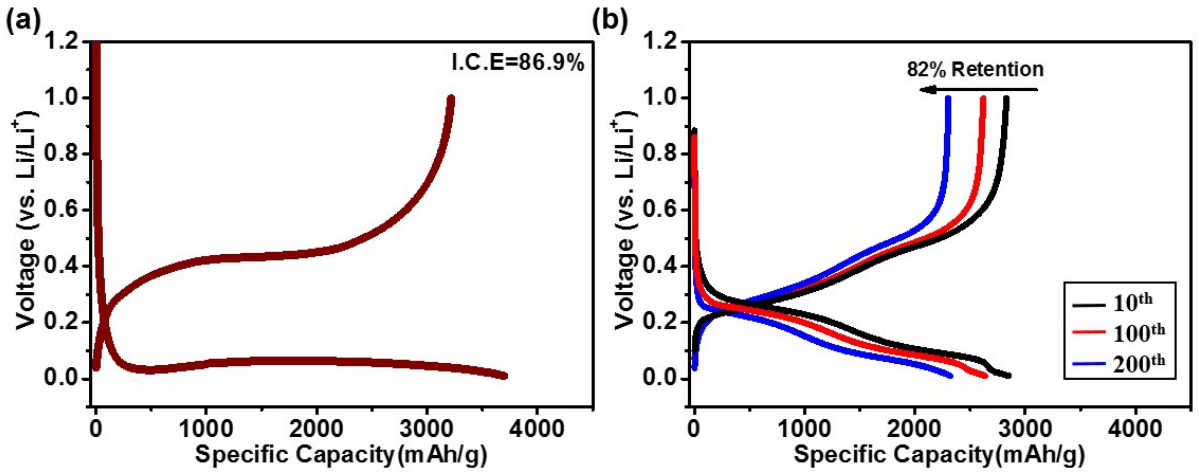

Fig. S12 (a) First galvanostatic graph of EB-1 electrode (ICE=86.9%) and (b) galvanostatic graph from 10th to 200th cycle with retaining 82% of its original capacity.

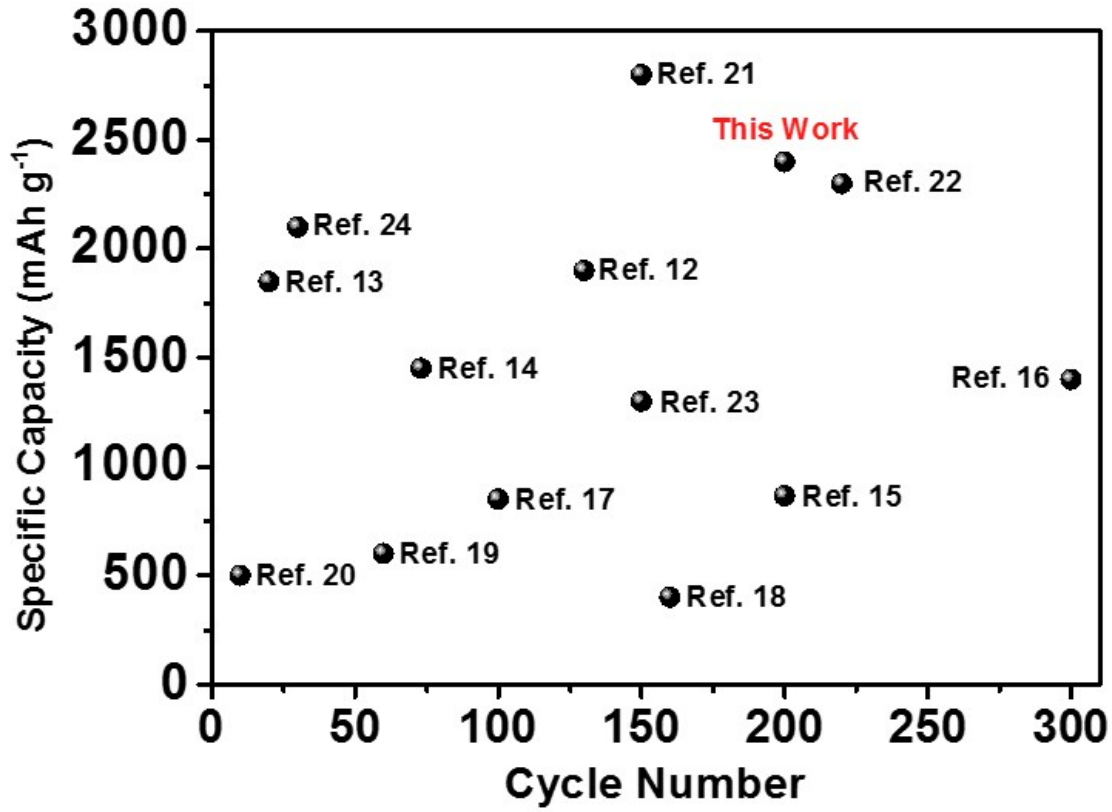

Fig. S13 The comparison of electrochemical performance of EB-1 electrode with previously reported Si electrodes using commercial micro-size Si.

Fig. S14 (a) Optical image of 0.2 g nano-Si, SiMP, and [SiMP+GO] composite and (b) cross-section image of EB-1 electrode with a Si mass loading of 1.42 mg cm^{-2}.

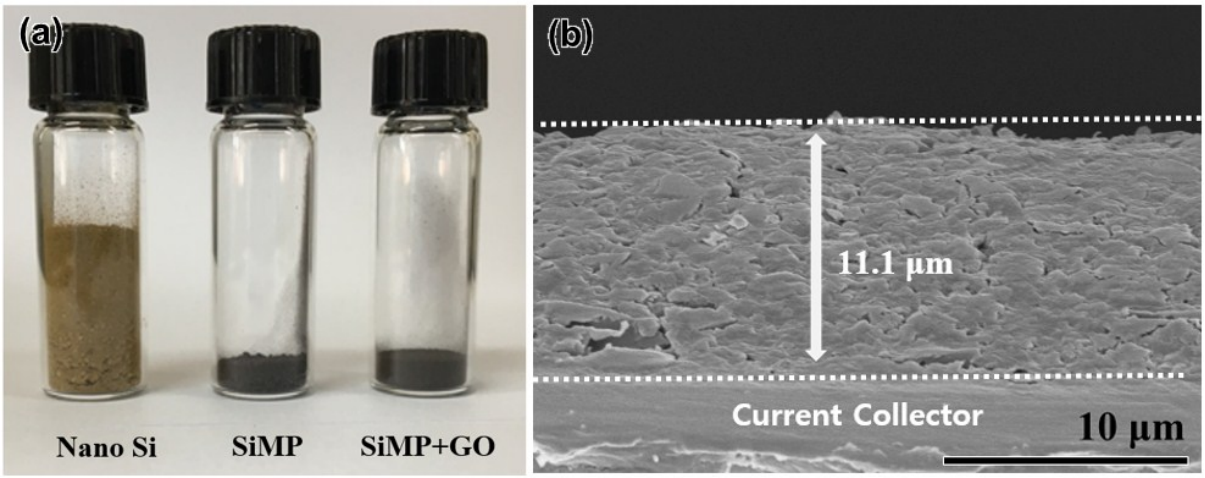

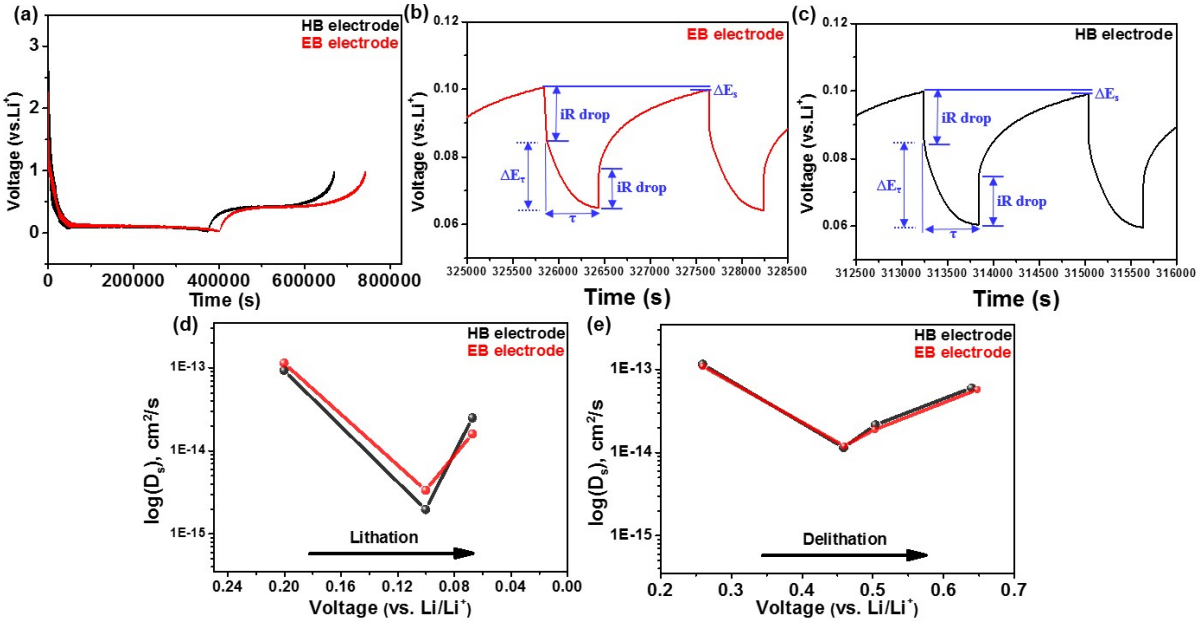

Fig. S15 (a) Voltage/time GITT graph for HB and EB electrodes for the first cycle. The voltage profile with a schematic labeling of different parameters for (b) HB and (c) EB electrodes. The calculated of Li^+ ion mobility of HB and EB electrodes during (d) lithiation and (e) delithiation.

The diffusion mobility has been calculated based on the equation; $D_{Li}+ = \frac{4}{\pi\tau}(\frac{n_m V_M}{S})^2(\frac{\Delta E_S}{\Delta E_\tau})^2$, where τ is duration of the current pulse (s), n_m is number of moles, V_m is the molar volume of the electrode, S is electrode/electrolyte contact area (cm^2), ΔE_s is the steady-state voltage change, and ΔE_t is voltage change during constant current pulse.

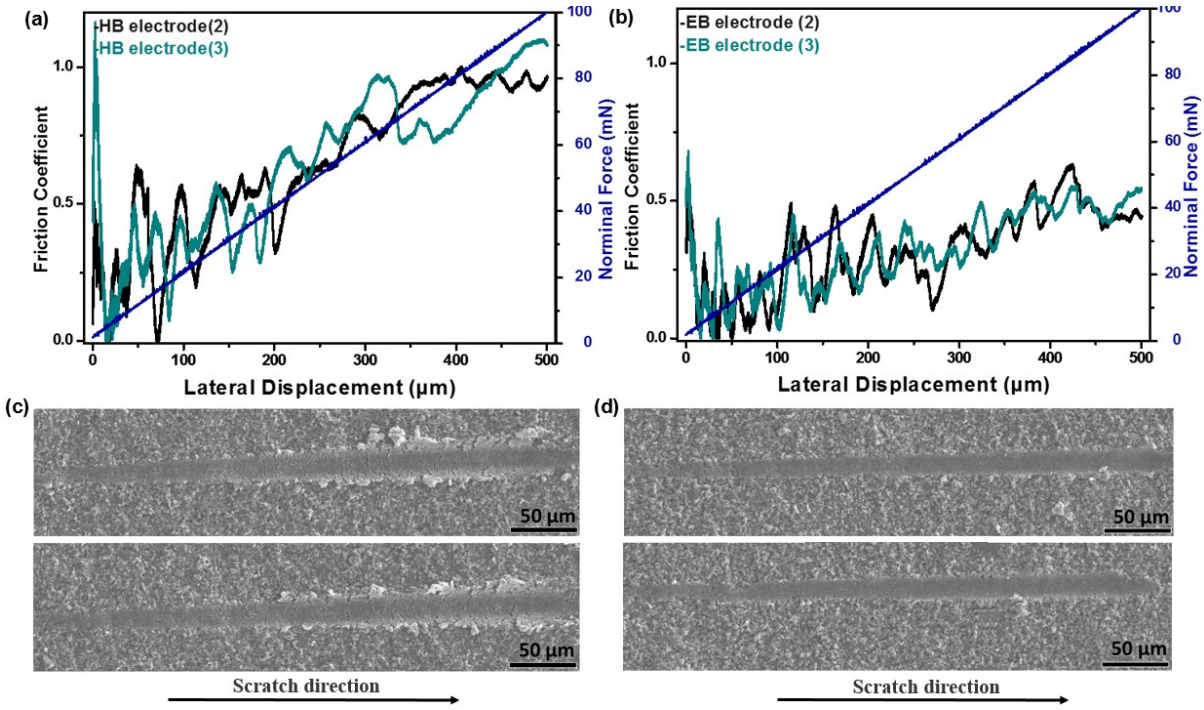

Fig. S16 Micro scratch test reproducibility for (a) HB electrode (b) EB electrode and its scratch image by SEM for (c) HB electrode and (d) EB electrode.

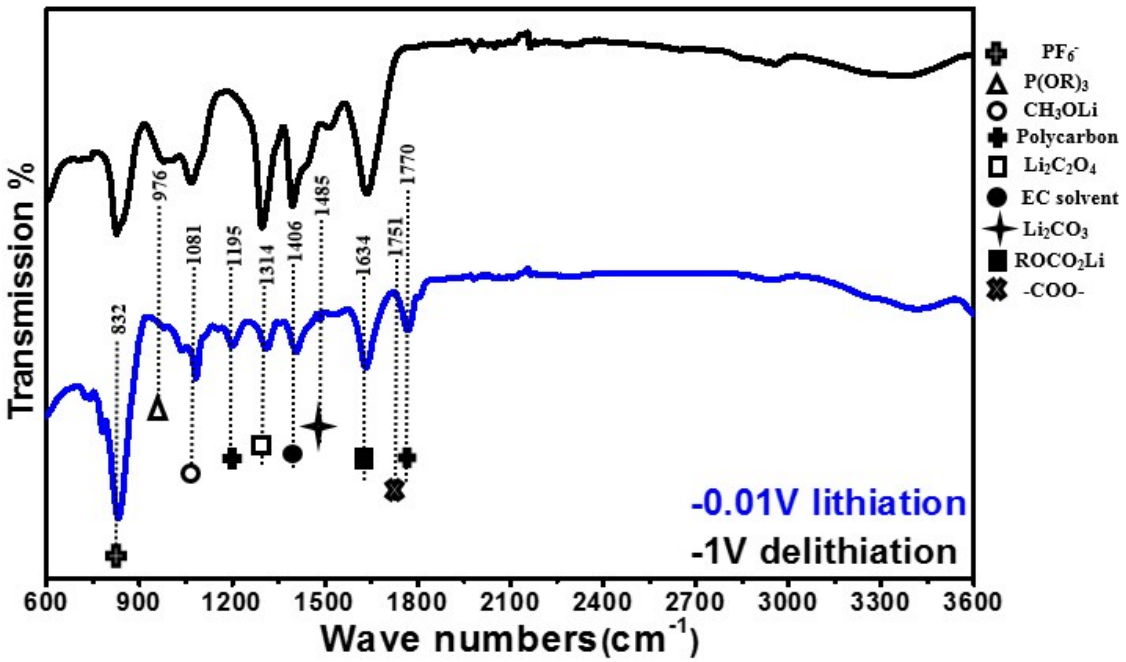

Fig. S17 FT-IR spectra of EB-1 electrode after first lithiation/delithiation. The peaks for binder cannot be detected due to the secondary phases such as SEI layer, electrolyte salt, and electrolyte solvent.[25,26]

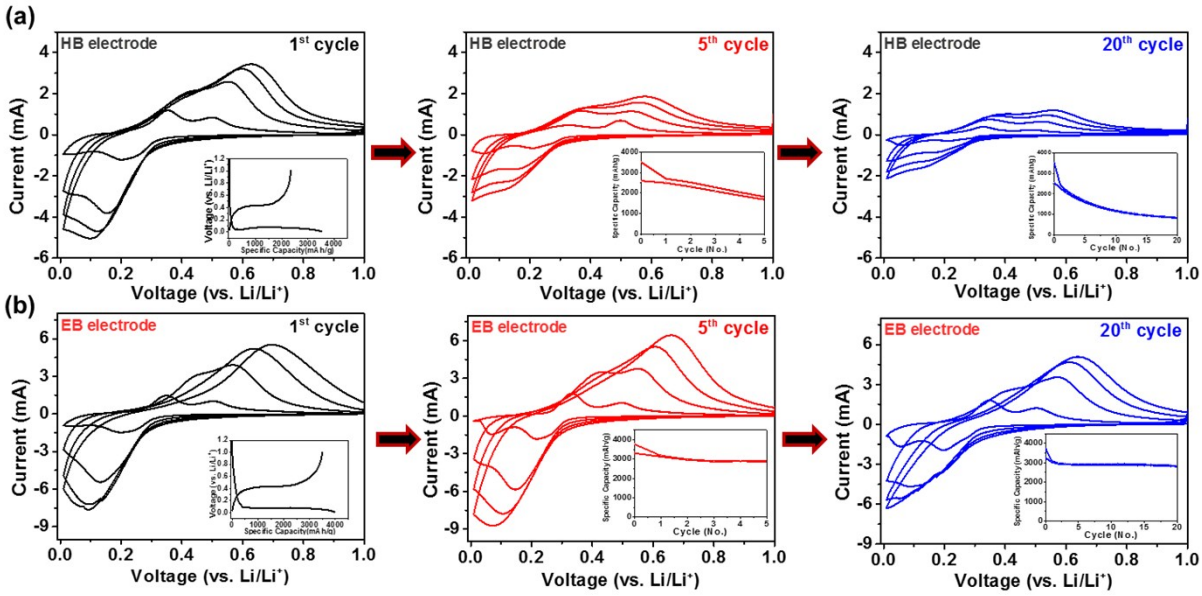

Fig. S18 Cyclic voltammetry for (a) HB and (b) EB electrodes at different scan rates from 0.1 to 1.0 mV s^{-1} after 1st, 5th, and 20th cycles.

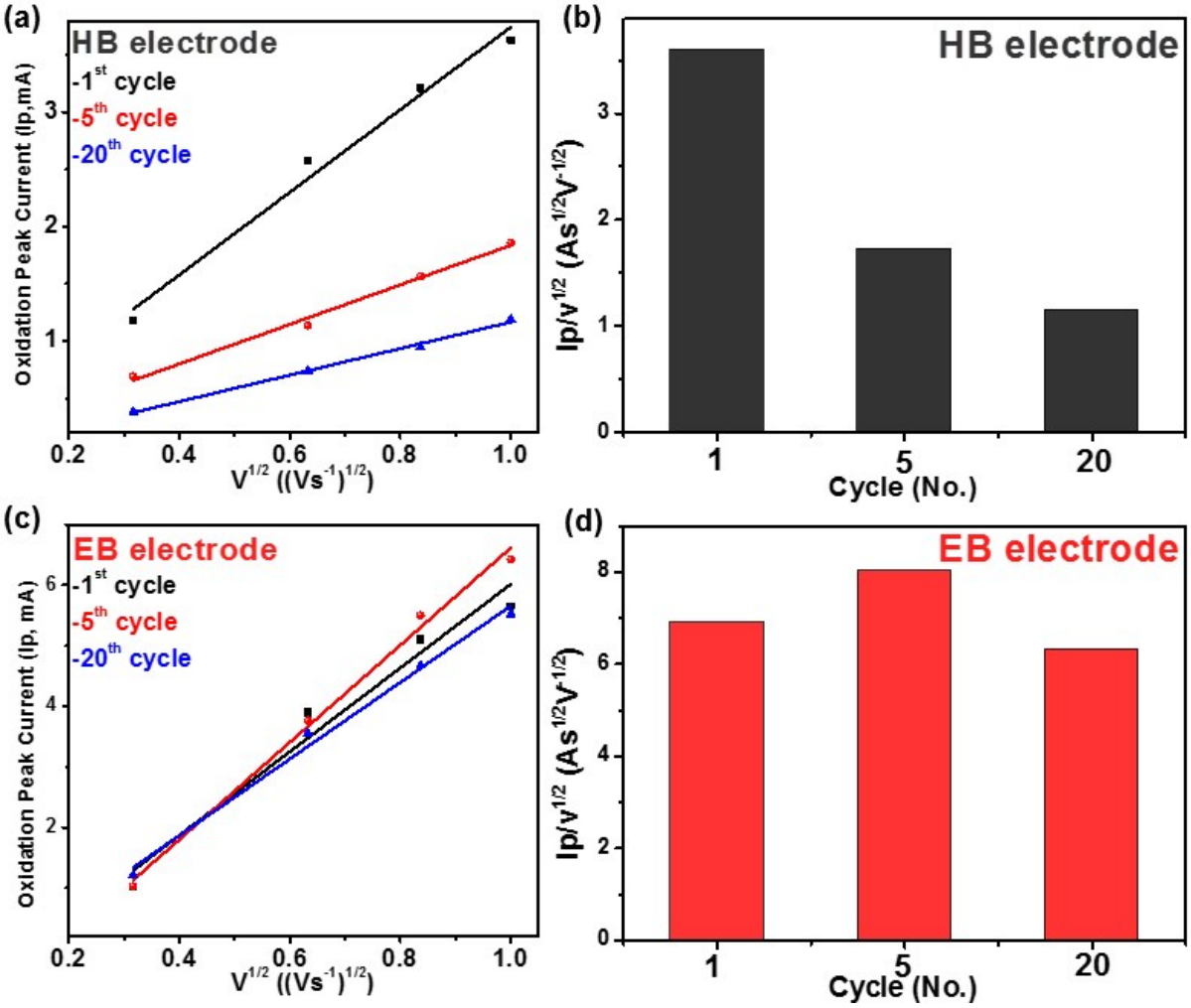

Fig. S19 Oxidation peak current versus root scan rate for (a) HB electrode and (b) its change of $I_p/v^{1/2}$ upon cycle. Oxidation peak current versus root scan rate for (c) EB electrode and (d) its change of $I_p/v^{1/2}$ upon cycle.

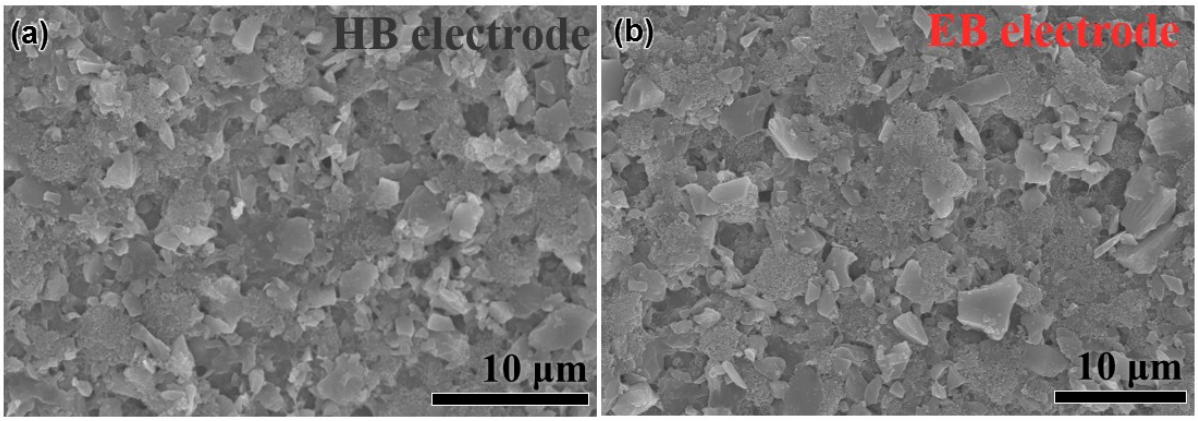

Fig. S20 SEM images of pristine HB and EB electrodes.

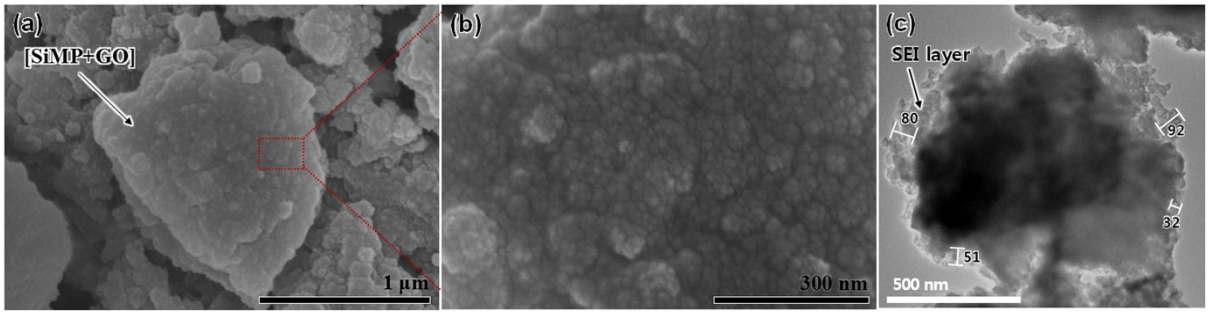

Fig. S21 (a), (b) SEM and (c) TEM images of EB electrode covered with thin SEI layer. Number on TEM image indicates the thickness of SEI layer with a unit in nanometer.

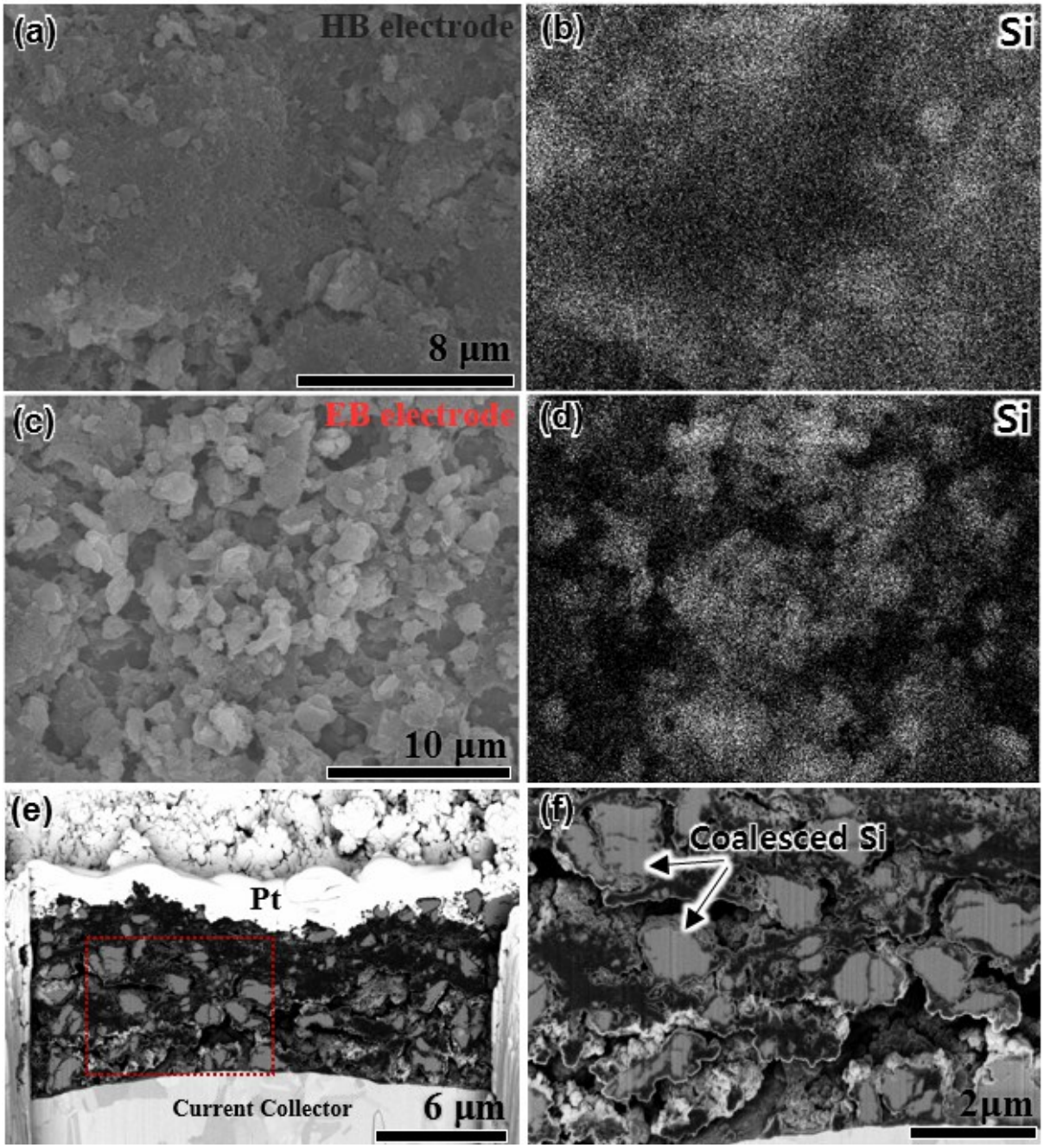

Fig. S22 SEM and EDS images of SEI layer etched after cycled electrodes for (a), (b) HB electrode and (c), (d) EB electrode, respectively. (e), (f) SEM observation of cross-sectioned EB electrode by back-scattered electron (BSE) mode. As the high atomic number objective displays the enhanced brightness, Si particles can be clearly visualized compared to carbonaceous materials.[21] BSE images showed that the pulverized Si was coalesced inside GO-PAA cage with a particle size of 1~3 μm.

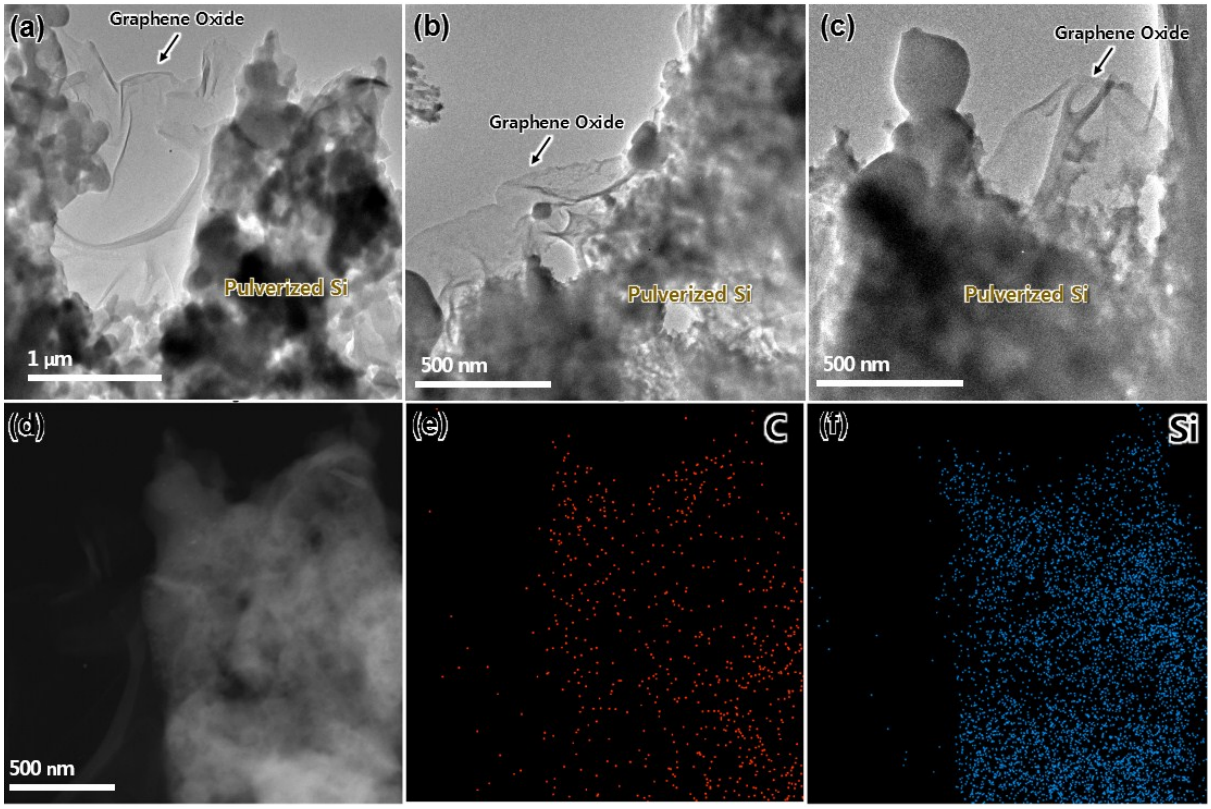

Fig. S23 (a), (b), (c) TEM images of the after cycled EB-1 electrode, where GO covering the pulverized Si can be seen. (d) STEM and (e), (f) EDS mapping images of after cycled EB-1 electrode. For the TEM and STEM images, EB-1 electrode was selected to clearly distinguish the pulverized Si from the Super-P.

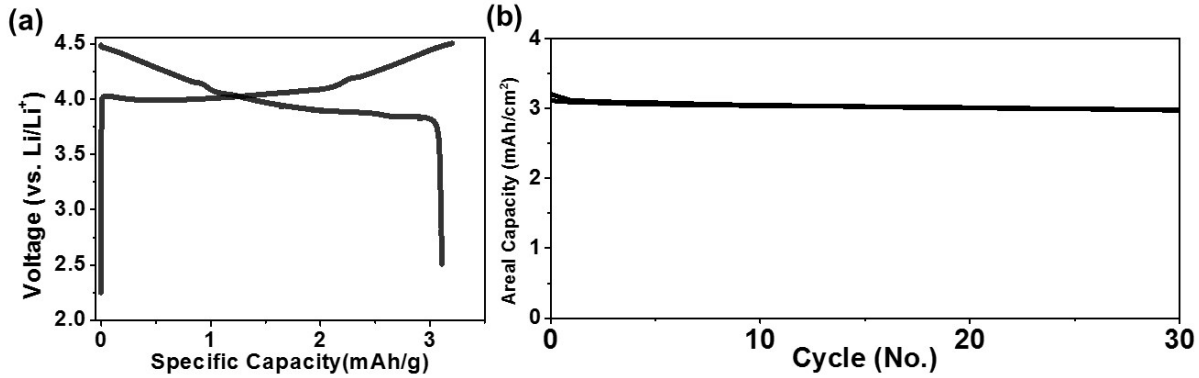

Fig. S24 (a) Galvanostatic graph of 1st cycle at current density of 0.3C and (b) cycle performance of $LiCoO_2$ (LCO) cathode half-cell between 2.5 and 4.5 V at the current density of 0.3C (1C=2.5 mAh cm^{-2}).

Notes and references

[1] Y. Li, K. Yan, H.-W. Lee, Z. Lu, N. Liu, Y. Cui, *Nature Energy*, 2016, **1**, 15029.

[2] Y. Zhang, Z. Mu, J. Lai, Y. Chao, Y. Yang, P. Zhou, Y. Li, W. Yang, Z. Xia, S. Guo, *ACS Nano*, 2019, **13**, 2167-2175.

[3] J. Yang, Y. Wang, W. Li, L. Wang, Y. Fan, W. Jiang, W. Luo, Y. Wang, B. Kong, C. Selomulya, H. K. Liu, S. X. Dou, D. Zhao, *Adv. Mater*., 2017, **29**, 1700523.

[4] T. Ma, X. Yu, H. Li, W. Zhang, X. Cheng, W. Zhu, X. Qiu, *Nano Lett*., 2017, **17**, 3959-3964.

[5] G. Zhu, Y. Gu, Y. Wang, Q. Qu, H. Zheng, *J. Alloys Compd*., 2019, **787**, 928-934.

[6] B. Han, Y. Yang, X. Shi, G. Zhang, L. Gong, D. Xu, H. Zeng, C. Wang, M. Gu, Y. Deng, *Nano Energy*, 2018, **50**, 359-366.

[7] G. Carbonari, F. Maroni, A. Birrozzi, R. Tossici, F. Croce, F. Nobili, *Electrochim. Acta*, 2018, **281**, 676-683.

[8] L. Lin, Y. Ma, Q. Xie, L. Wang, Q. Zhang, D.-L. Peng, *ACS Nano*, 2017, **11**, 6893-6903.

[9] Q. Xu, J.-Y. Li, J.-K. Sun, Y.-X. Yin, L.-J. Wan, Y. -G. Guo, *Adv. Energy. Materials*, 2017, **7**, 1601481.

[10] S. Choi, T.-W. Kwon, A. Coskun, J. W. Choi, *Science*, 2017, **21**, 279-283.

[11] R. Teki, M. K. Datta, R. Krishnan, T. C. Parker, T.-M. Lu, P. N. Kumta, N. Koratkar, *Small*, 2009, **5**, 2236-2242

[12] C. Wang, H. Wu, Z. Chen, M. T. McDowell, Y. Cui, Z. Bao, *Nature Chem*., 2013, **5**, 1042-1048.

[13] B. M. Bang, H. Kim, H.-K. Song, J. Cho, S. Park, *Energy Environ. Sci*., 2011, **4**, 5013-5019.

[14] D. Wang, M. Gao, H. Pan, J. Wang, Y. Liu, *J. Power Sources*, 2014, **256**, 190-199.

[15] R. Hu, W. Sun, Y. Chen, M. Zeng, M. Zhu, *J. Mater. Chem. A*, 2014, **2**, 9118-9125.

[16] Y. Li, K. Yan, H. –W. Lee, Z. Lu, N. Liu, Y. Cui, *Nature Energy*, 2016, **1**, 15029.

[17] M. N. Obrovaca, L. J. Krauseb, *J. Electrochem. Soc*., 2007, **154**, A103-A108.

[18] Z. Chen, V. Chevrier, L. Christensen, J. R. Dahna, *Electrochem. Solid-State Lett*., 2004, **10**, A310-A314.

[19] W.-R. Liu, Z.-Z. Guo, W.-S. Young, D.-T. Shieh, H.-C. Wu, M.-H. Yang, N.-L. Wu, *J. Power Sources*, 2005, **140**, 139-144.

[20] J. H. Ryu, J. W. Kim, Y.-E. Sung, S. M. Oh, *Electrochem. Solid-State Lett*., 2004, **7**, A306-A309.

[21] S. Choi, T.-W. Kwon, A. Coskun, J. W. Choi, *Science*, 2017, **357**, 279-283.

[22] Z. Xu, J. Yang, T. Zhang, Y. Nuli, J. Wang, S.-I. Hirano, *Joule*, 2018, **2**, 950-961.

[23] T. Munaoka, X. Yan, J. Lopez, J. W. F. To, J. Park, J. B.-H. Tok, Y. Cui, Z. Bao, *Adv. Energy. Mater*., 2018, **8**, 1703138.

[24] M. Wu, J. E. C. Sabisch, X. Song, A. M. Minor, V. S. Battaglia, Gao Liu, *Nano Lett.,* 2013, **13**, 5397−5402.

[25] C. C. Nguyen, T. Yoon, D. M. Seo, P. Guduru, Brett L. Lucht, *ACS Appl. Mater. Interfaces,* 2016, **8**, 12211-12220.

[26] V. Etacheri, O. Haik, Y. Goffer, G. A. Roberts, I. C. Stefan, R. Fasching, D. Aurbach, *Langmuir*, 2012, **28**, 965-976.